Influence of contour parameters on the surface roughness of fine channels produced by powder bed fusion-laser beam

Citation for the original published paper (version of record):

Tiwari, J., Malladi, B., Mishurova, T. et al (2026). Influence of contour parameters on the surface roughness of fine channels produced by powder bed fusion-laser beam. Vacuum, 246. http://dx.doi.org/10.1016/j.vacuum.2026.115085

Vacuum 246 (2026) 115085

Contents lists available at ScienceDirect

Vacuum

journal homepage: www.elsevier.com/locate/vacuum

Influence of contour parameters on the surface roughness of fine channels produced by powder bed fusion-laser beam

Jitendar Kumar Tiwari [a,b], Bala Malladi [a], Tatiana Mishurova [c,d], Tobias Fritsch [c], Lars Nyborg [a], Yu Cao [a,*]

[a] Department of Industrial and Materials Science, Chalmers University of Technology, Gothenburg, Sweden
[b] Mechanical Engineering Discipline, PDPM Indian Institute of Information Technology, Design and Manufacturing, Jabalpur, M.P, 482005, India
[c] Bundesanstalt für Materialforschung und-prüfung (BAM), Berlin, Germany
[d] Helmholtz-Zentrum Berlin für Materialien und Energie GmbH, Berlin, Germany

ARTICLE INFO

Keywords:
Additive manufacturing
Surface roughness
X-ray computed tomography
Surface profilometry

ABSTRACT

Surface roughness strongly influences the performance of fine internal channels in additively manufactured components. This study investigates how contour process parameters affect the surface finish of 1 mm-diameter channels produced by powder bed fusion–laser beam (PBF-LB). Five contour parameter sets with progressively increasing laser energy density (LED) were applied, while keeping infill parameters constant. Surface roughness was evaluated using surface profilometry, X-ray computed tomography (XCT), and optical microscopy (OM). Profilometry and OM provided localized measurements, whereas XCT captured full-channel roughness along the build direction. Results show that increasing LED initially reduces surface roughness due to improved melting and removal of partially fused particles, reaching optimal smoothness at an intermediate LED. Further LED increase causes roughness to rise again, attributed to balling and dross formation. Optical cross-sections depicted these trends, and XCT measurements closely matched profilometry data. The findings in this study highlight a trade-off between surface quality and dimensional accuracy, as higher LEDs improve smoothness but reduce channel diameter. This work establishes an optimal contour LED range for minimizing as-built surface roughness in fine internal channels, which can enhance the functional performance of PBF-LB components in aerospace, medical, and energy applications.

1. Introduction

Industrial adaptation of additive manufacturing (AM) is growing rapidly since it offers an effective solution for producing components with complex geometries [1]. The design freedom in AM allows it to manufacture complex structures such as lattice architectures [2], customized implants [3], topologically optimized parts [4] and internal channels embedded parts [5] which could previously be imagined but were not possible to fabricate due to limitations associated with conventional manufacturing techniques. Among these, internal channels embedded in the part, which is being recommended for space and for other sophisticated scenarios [6], are particularly important. However, the surface roughness inherited to AM produced channels remained a major challenge [7]. In general, there are two types of surface roughness present in AM printed parts, i.e., top surface and side surface roughness. The side surface roughness is of high importance as it contains the information of each layer. When dealing with inclined surfaces facing downward, the laser beam can penetrate the underlying powder, resulting in dross formation which is the roughest surface in any powder bed fusion-laser beam (PBF-LB) printed part. Therefore, it is important to design a part in such a way that it contains less inclined surfaces. The design-related compensation strategies during AM of fine channels was demonstrated previously [8,9]. In general, the side surface roughness of the components manufactured by directed energy deposition (DED), PBF- electron beam, PBF-LB and binder jetting technology (BJT), are in decreasing order [10]. However, PBF-LB is generally recommended over the DED, PBF- e^- beam and BJT due to several advantages including dimensional accuracy, design freedom, good processability and mechanical properties [11]. There are several techniques that can be used to measure surface roughness. Profilometry is a commonly used one to analyze surface topography of any component. X-ray computed tomography (XCT) allows the evaluation of surface roughness of the

---

* Corresponding author. Department of Industrial and Materials Science, Chalmers University of Technology, Gothenburg, 412 96, Sweden.
E-mail address: yu.cao@chalmers.se (Y. Cao).

https://doi.org/10.1016/j.vacuum.2026.115085
Received 29 October 2025; Received in revised form 23 December 2025; Accepted 10 January 2026

Table 1
Chemical composition of as-received SS 316 L powder.

Element	Cr	Ni	Mo	Si	Mn	C	S	P	Fe
Content (wt. %)	17.5–18	12.5–13	2.25–2.5	Max. 0.75	Max. 2.00	Max. 0.003	Max. 0.010	Max. 0.025	Balance

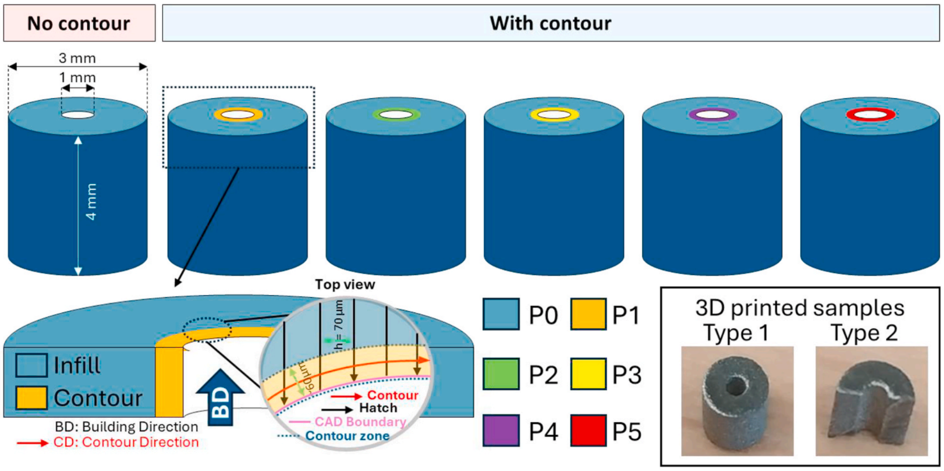

Fig. 1. Schematic of samples without (P0) and with contour (P1 - P5) along with type 1 and type 2 3D printed samples in the right bottom corner.

Table 2
Process parameters of printed samples with and without contour.

Sample name	Parameters		
	Laser Power (P) (W)	Scan speed (v) (mm/s)	Linear energy density (P/v) (J/mm)
P0 (No contour)	77	827	0.093
P1	47	800	0.058
P2	57	700	0.081
P3	67	600	0.111
P4	77	500	0.154
P5	87	400	0.217

internal channels and fine geometrical features non-destructively and obtain not only classic surface roughness parameters but also features hidden under the surfaces (such as re-entrant features). Klingaa et al. has demonstrated the measurement of surface roughness of the internal channels using this technique and evaluated the influence of surface roughness of the channels on its cooling ability defined by Nusselt number [12]. The influence of laser treatment on the surface characteristics at microscopic level is confirmed previously [13,14].

The surface roughness inherited to as-built parts may largely influence its mechanical (especially fatigue) and functional properties [15]. For components with internal channels, minimizing the roughness of the channel's internal surfaces is especially critical, since large roughness affects flow characteristics, pressure drop, heat transfer, wear and erosion [12,16] when exposed to a flowing fluid. There are two ways to minimize the surface roughness of additively manufactured parts: a) alteration of process related parameters [17–20], and b) post-processing [21–23]. Improving the surface finish directly during printing by tailoring the parameters may reduce the need for post-processing, which is particularly advantageous for components with internal flow channels. Post-processing is often ineffective for the parts with complex geometry. When applicable, it increases the cost and lead time of the final part. Therefore, minimizing the surface roughness in as-printed condition is highly desirable. Several reports are available on the influence of process parameters on surface roughness in PBF-LB process [24–26]. While early studies attributed surface roughness in PBF-LB process primarily to layer thickness, later research showed that many other parameters play significant roles. These include laser re-melting or contouring [27], laser incidence, laser focus shift [28], hatch spacing [29], powder reuse [30], particle size distribution [31], scanning strategy [32] etc. Among these parameters, contouring is the most suitable strategy for improving the quality of side surfaces, especially for parts containing internal channels. A number of reports have been published to demonstrate the influence of contour on the surface roughness of the as printed parts [33,34]. Wang et al. reported a reduction of ~50 % in the surface roughness (R_a) value of the Ti6Al4V thin-walled part manufactured using PBF- e^- beam when a dashed-scan contouring strategy was applied [35]. The reduction in the surface roughness (R_a) below ~ 1 μm of PBF-LB processed Zr-based bulk metallic glass was achieved by increasing the laser power of the contour scan [27]. Various contouring strategies, including pre-contour or post-contour have been investigated in the literature. It has been reported that the pre-contour results in better surface finish of the downskin surface compared to post-contour [36]. Moreover, the contour scan can significantly enhance the dimensional accuracy of the thin geometry such as fine channels or lattice struts by tailoring it's laser process parameters [37]. To effectively minimize the side surface roughness, careful selection of contour scan parameters such as laser power, scan speed, laser energy density etc. is of high importance.

Although numerous studies have explored the influence of contour parameters on surface roughness in PBF-LB process, most of them have focused either on external surfaces or on simplified geometries. There is still a lack of comprehensive investigation specifically targeting the surface roughness of fine internal channels. Furthermore, while XCT has emerged as a powerful non-destructive technique for internal surface evaluation, it has not been sufficiently integrated with other surface characterization methods such as optical microscopy (OM) and surface profilometry for cross-validation of roughness data. A deeper understanding of how contouring strategies affect internal surface morphology and a reliable methodology to quantify roughness within such features are still needed to enable precision manufacturing.

The objective of this study is to systematically investigate the influence of laser contour scan energy density on the side surface roughness of internal channels manufactured via PBF-LB, while keeping the infill process parameters constant. The study aims to evaluate and correlate

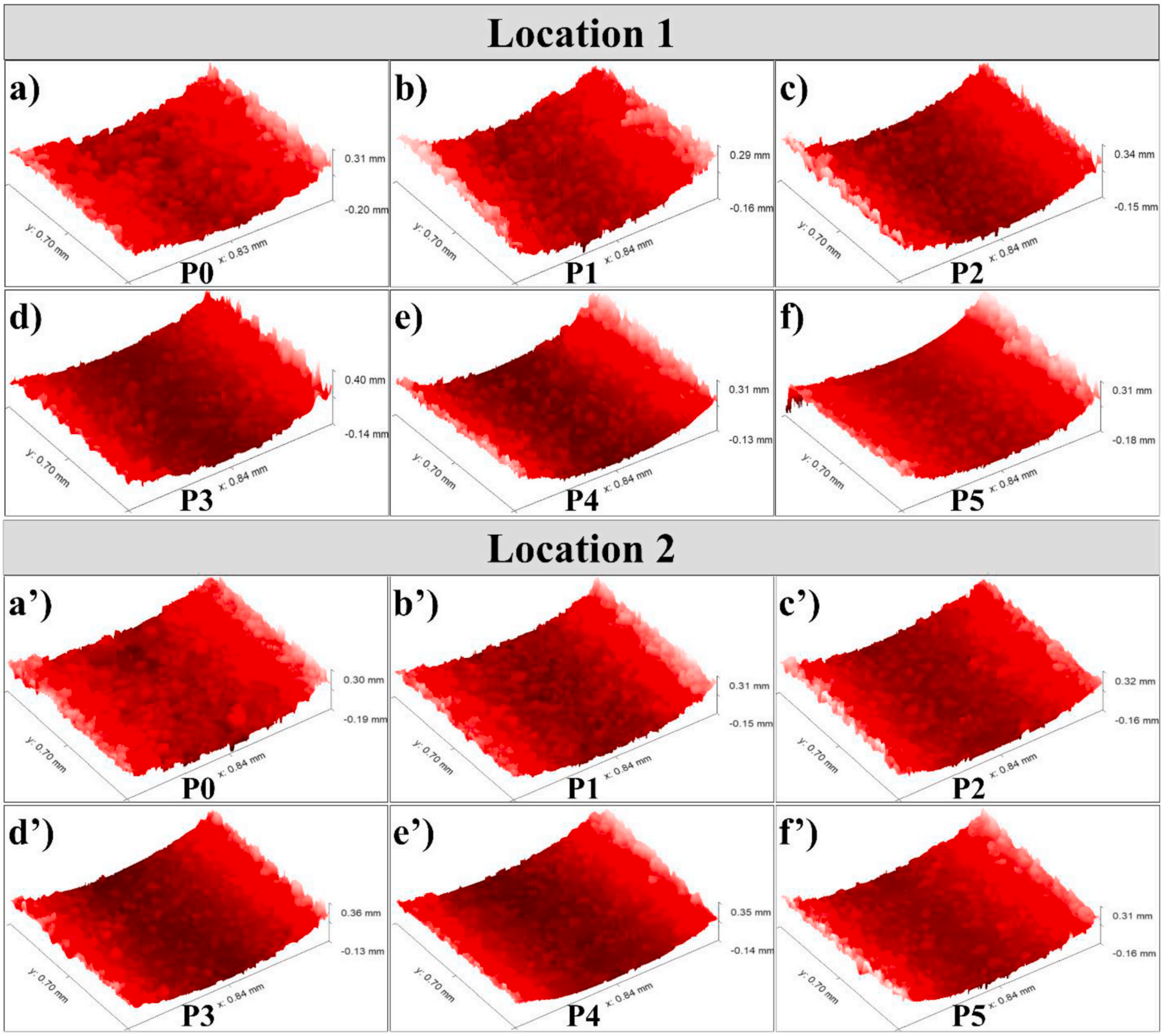

Fig. 2. Surface profilometry of samples a) P0, b) P1, c) P2, d) P3, e) P4, f) P5 at location 1 and a') P0, b') P1, c') P2, d') P3, e') P4, f') P5 at location 2.

surface roughness data obtained from surface profilometry and XCT techniques. Additionally, OM was used to examine tomographic slices and validate surface roughness obtained by other two techniques. By comparing the surface roughness of contour-processed and no-contour counterparts, this study identifies the optimal laser energy density (LED) for contour that minimizes side surface roughness, thereby enhancing surface finish of parts with fine internal channels in as-printed condition. This work contributes toward the broader goal of enabling more effective use of PBF-LB for functional components in aerospace, medical, and energy sectors where internal channel performance is critical.

2. Experimental procedure

2.1. Materials and methods

Gas atomized SS 316 L powder with size between 15 and 45 μm, supplied from Höganas AB, was used in this study. The SS 316 L powder was dried in low vacuum at 100 °C for 4 h to avoid hydrogen uptake and other impurities during laser fusion of material which would likely have an insignificant effect on the material properties [38]. The composition and particle size distribution of the powder is summarized in Table 1.

An EOS M100 machine was used to print two types of cylindrical samples named as type 1 and type 2 with same infill and different contour parameters as shown in Fig. 1. The samples have an internal diameter of 1 mm, an external diameter of 3 mm and height of 4 mm. The laser power (*P*), scan speed (*v*) and linear energy density (*P*/*v*) values of different contour parameters are summarized in Table 2. The linear energy density of the contour parameters P1 to P5 increased from ~0.058 to ~0.217 J/mm. The layer thickness and hatch distance were 20 μm and 70 μm, respectively. The diameter of Yb fiber laser beam was fixed to 40 μm and the wavelength was 1080 nm. The oxygen content in the building chamber was maintained below 0.1 vol % (1000 ppm) by circulating the high purity argon (~99.99 %) with a blow rate of 35 L/min. Oxygen levels in the range of 20–1000 ppm have no significant effect on the chemical composition and properties of the SS 316 L [39]. In addition, no support structure was required since the axis of the cylindrical hole (channel) was oriented parallel to the building direction.

2.2. Characterization

As-printed samples were characterized using surface profilometry, X-ray computed tomography (XCT) and optical microscopy (OM) to measure the surface roughness of the internal curved surface of the channel. Type 1 and type 2 samples were used for XCT and surface profilometry, respectively. The slices of type 1 samples cut perpendicular to the building direction, were examined further under OM to provide complementary information. The data acquisition and analysis parameters of these three techniques are as follows.

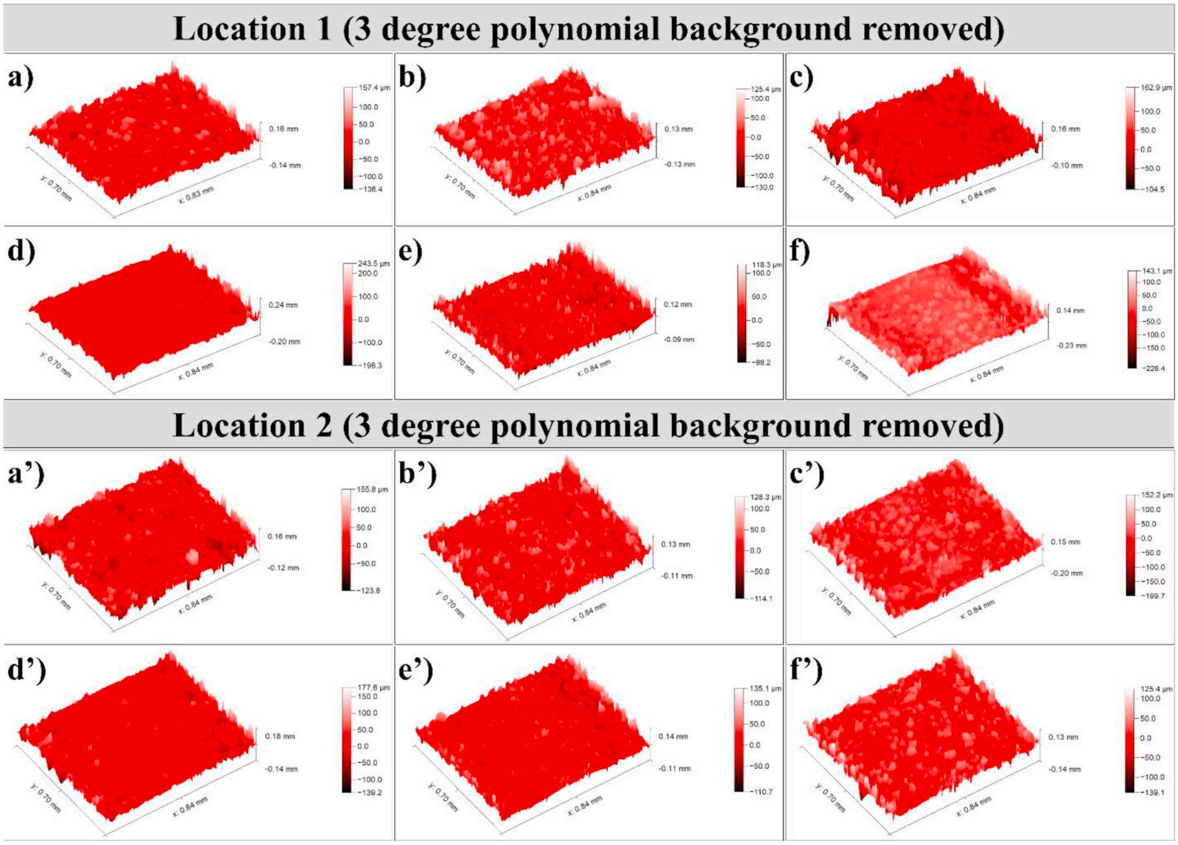

Fig. 3. Surface profilometry of samples after removing 3-degree polynomial background a) P0, b) P1, c) P2, d) P3, e) P4, f) P5 at location 1 and a') P0, b') P1, c') P2, d') P3, e') P4, f') P5 at location 2.

2.2.1. *Surface profilometry measurements*

The samples were cleaned with ethanol and dried before measurements. The surface profiles were obtained at two locations of type 2 samples under each condition using a Sensofar Sneox system, in confocal mode with green light at 20X epi objective 0.45 NA. The reproducibility of the results contains a deviation of approximately ±20 nm. Gwyddion, an open-source software, was used to post-process the obtained data [40]. The roughness parameters including mean surface roughness (S_a, the areal equivalent to R_a), root mean square (RMS) surface roughness (S_q, the areal equivalent to R_q), skewness (S_{sk}) and kurtosis (S_{ku}) were measured according to ISO 25178 [41]. These parameters are formulated in equations (1)–(4) where *Z(x,y)* is the height value of each acquired points and *A* is the acquired area.

$$S_a = \frac{1}{A}\iint_A |Z(x,y)|dx \tag{1}$$

$$S_q = \sqrt{\frac{1}{A}\iint_A Z^2(x,y)dxdy} \tag{2}$$

$$S_{sk} = \frac{1}{Sq^3}\left[\frac{1}{A}\iint_A |Z^3(x,y)|dxdy\right] \tag{3}$$

$$S_{ku} = \frac{1}{Sq^4}\left[\frac{1}{A}\iint_A |Z^4(x,y)|dxdy\right] \tag{4}$$

The curved profiles correspond to the cylindrical curved surface of internal channels were obtained by profilometry. To simplify the extraction of statistical data, a three-degree polynomial was subtracted from the curved profile to obtain the flat profile. Surface profilometry provides higher vertical resolution but it is applied only to the central region of the channel wall to avoid distortions near the curved edges. Only the x range of 0.3–0.5 mm from the acquired flat profile was considered for the quantitative evaluation (S_a, S_q, S_{sk} and S_{ku}) since the accuracy of the acquired data is higher in the central region than in the side curved region.

2.2.2. *X-ray Computed Tomography (XCT) measurements*

The XCT scans of the type 1 samples were conducted on a laboratory CT scanner (GE v|tome|x 300 L) using a transmission target. A voltage of 130 kV and a current of 60 μA were applied to the X-ray tube. Typically, the spatial resolution in XCT scans is defined as 2–3 voxels. Since the reconstructed voxel size was 2 μm, the resolution is expected to be around 4–6 μm. As the dominant asperities on the internal surfaces (typically 5–25 μm) are well above this threshold, XCT scan results do not affect the validity of the obtained surface roughness. The gray value reconstruction of the sample was first segmented into material and background by using the advanced surface determination implemented in Volume Graphics software. The surface was converted into a point cloud with the spatial resolution of the voxel size (2 μm). Afterwards the point cloud from Cartesian was converted into cylindrical coordinate system, to extract the line profiles along the length of the channel. The line profile width was set to 1°, so a total of 180 line profiles were extracted for each channel, corresponding to half of the channel's curved surface. The average surface roughness R_a was then obtained according to equation (5).

$$R_a = \frac{1}{N}\sum_{i=1}^{N}\left|\rho_i^{\theta}(z) - \rho_{mean}^{\theta}\right| \tag{5}$$

Where.

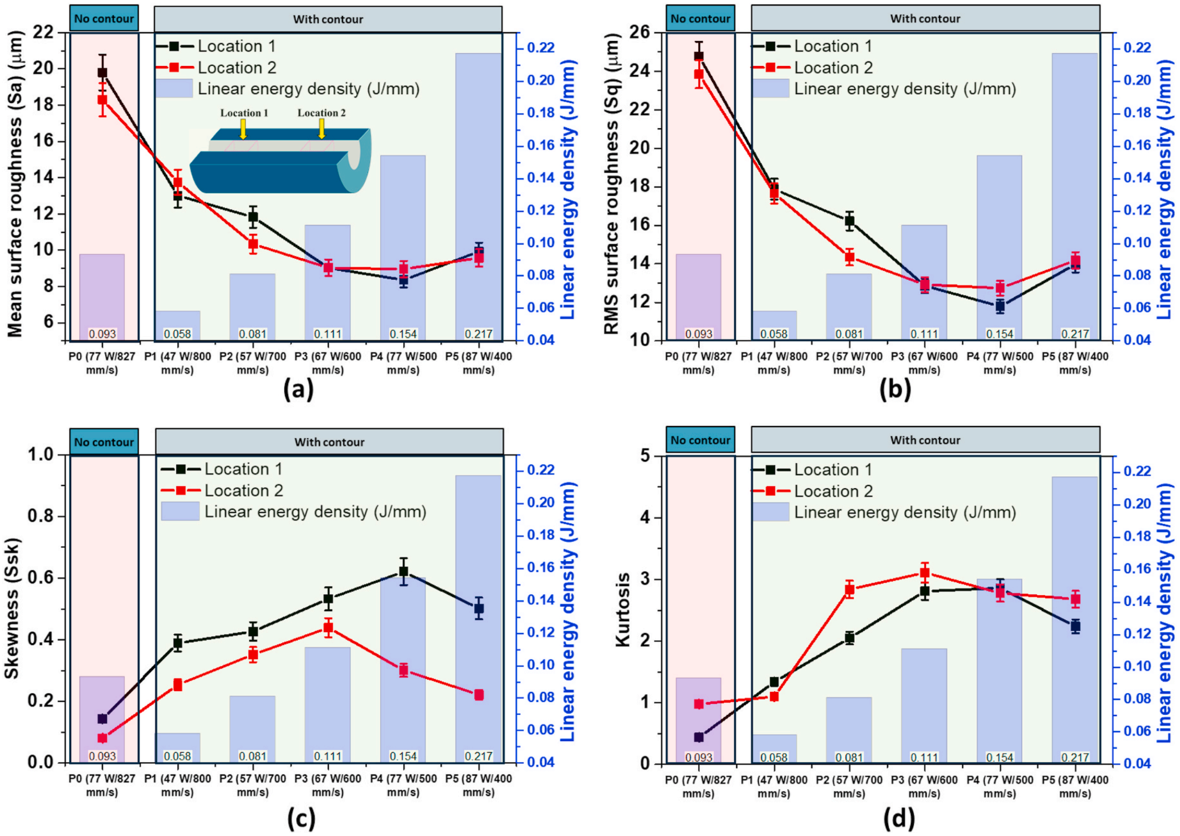

Fig. 4. a) Mean surface roughness (S_a) b) RMS surface roughness (S_q) c) Skewness (S_{sk}) d) Kurtosis (S_{ku}) of P0-P5 samples along with respective different laser energy density or linear energy density (LED) values.

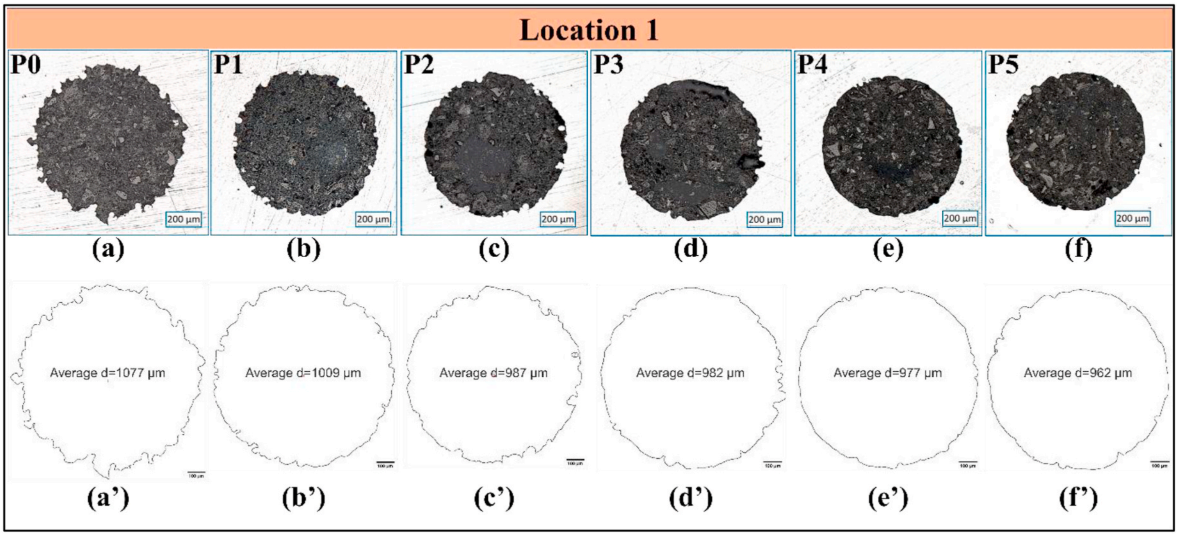

Fig. 5. Cross section of samples a) P0, b) P1, c) P2, d) P3, e) P4, f) P5 at location 1 perpendicular to building direction/axis of the hole(channel); Extracted profile of the hole boundary a') P0, b') P1, c') P2, d') P3, e') P4, f') P5 along with respective average channel diameter value.

R_a: Average surface roughness
N: number of points along the length
$\rho^{\theta}(z)$: distance of a cloud point from the mean value for a particular angular position θ
ρ^{θ}_{mean}: mean distance of cloud points along the profile at a given θ

2.2.3. Optical microscopy (OM) measurements

To observe the cross-section of channel perpendicular to building direction using OM, the type 1 samples were clamped in a clip before hot mounting and grinded using emery paper of grit sizes 400, 600, 1000 and 2000. These samples were further cloth polished using 9 µm, 3 µm and 1 µm diamond suspension. Note that the build direction of the samples was perpendicular to the polishing surface.

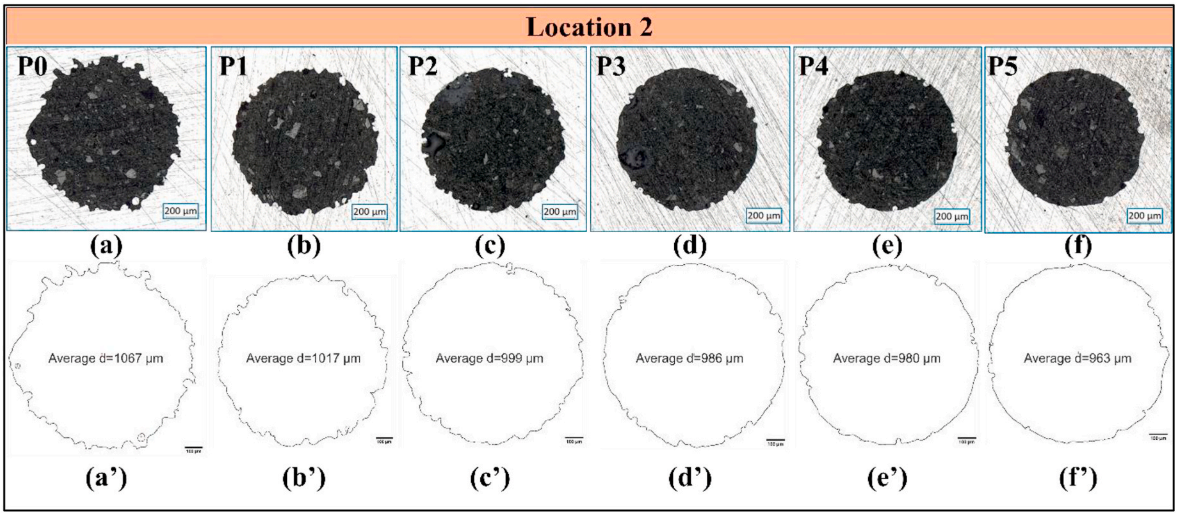

Fig. 6. Cross section of samples a) P0, b) P1, c) P2, d) P3, e) P4, f) P5 at location 2 perpendicular to building direction/axis of the hole(channel); Extracted profile of the hole boundary a') P0, b') P1, c') P2, d') P3, e') P4, f') P5 along with respective average channel diameter value.

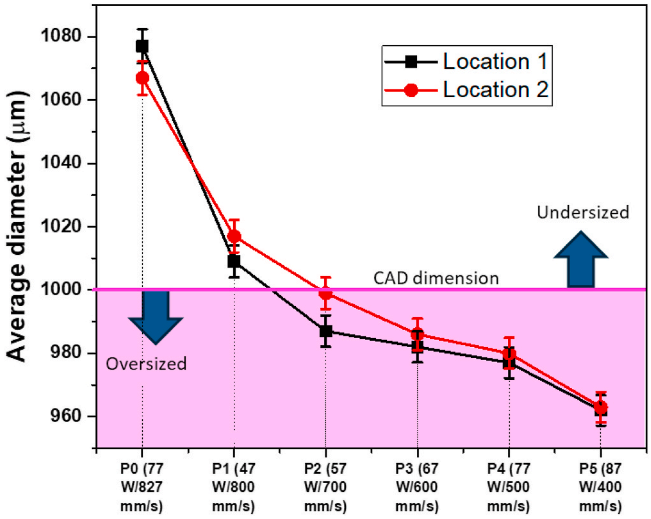

Fig. 7. Change in average channel diameter in the samples a) P0, b) P1, c) P2, d) P3, e) P4, and f) P5.

3. Results and discussion

3.1. *Surface roughness parameters S_a, S_q, S_{sk} and S_{ku} using surface profilometry*

The surface profilometry results of the type 2 samples acquired from two locations are shown in Figs. 2–4. Fig. 2 represents the curved profile of each sample whereas Fig. 3 represents the flat profile after subtracting the three-degree polynomial from the curved profile. The length (x) and width (y) of the acquired region is 0.84 mm and 0.70 mm, respectively. The quantitative information such as S_a, S_q, S_{sk} and S_{ku} was extracted from the flat profile and plotted against laser energy density of contour parameters (Fig. 4). The sample with no contour had a mean surface roughness (S_a) of 19.8 µm at location 1 and 18.3 µm at location 2, respectively. Note that P0 (laser power: 77 W and laser scan speed: 827 mm/s) is an infill parameter whereas P1 to P5 are contour parameters. When the contour strategy was implemented with same infill parameters, the mean surface roughness first decreases from P1 (13.01 µm at location 1 and 13.76 µm at location 2) to P4 (8.36 µm at location 1 and 8.96 µm at location 2) and then it slightly increases for P5 (9.93 µm at location 1 and 9.58 µm at location 2). Notice that the linear energy density of the contour increased progressively from P1 to P5. At low energy density, the surface roughness is mainly caused by the partially melted powder particles that become partly embedded in the melted contour region [17,42]. Increasing energy density of contour leads to the broader fusion zone which possesses less partially melted powder particles and significantly reduced surface roughness. At higher laser energy densities (greater than 0.217 J/mm), the melted region exhibited improved flowability of molten pool due to elevated melt pool temperatures. This increase in temperature extended the solidification time, thereby reducing surface tension compared to melt pools formed at lower energy densities [43,44]. It allows the molten liquid to spread and form dross. The dross formation due to heat accumulation in the melt pool at high energy density is reported by Zhang et al. [42]. Similarly, RMS surface roughness (S_q) showed a decreasing trend up to P4, followed by a slight increase.

Furthermore, skewness and kurtosis values were also plotted against laser energy density. Generally, skewness indicates the asymmetry of surface features, while kurtosis reflects their sharpness. Higher skewness and kurtosis values suggest greater asymmetry and sharper features on the surface, respectively. At low LED, the partially melted powder particles result in lower values of skewness and kurtosis (Fig. 4). As the LED increases, the formation of an asymmetric melt pool becomes more pronounced, and a smaller number of partially melted powder particles presents at the melt track. The formation of asymmetric melt pool occurs primarily due to uneven heat transfer along the contour. This results in increased skewness and kurtosis of the melt pool geometry. The asymmetry in heat transfer arises from the contrasting thermal properties at the contour boundary, where one side consists of fully solidified material and the other of loose metallic powder [45]. However, as LED continues to rise, the balling phenomenon may take over, leading to reduced asymmetry and sharpness, as well as a slight increase in S_a values. Further increases in energy density may ultimately result in higher surface roughness compared to what was observed at P5.

3.2. *Cross-section of channels using optical microscopy*

The optical microscopy of cross section of type 1 samples acquired from two locations are shown in Figs. 5 and 6. It is clearly depicted that the progressive increment in LED results in the smoother surface which is aligned with the observations from surface profilometry data. However, the actual channel diameter (CD) is deviated from the designed diameter i.e. 1000 µm. As per the surface profilometry data, the S_a value

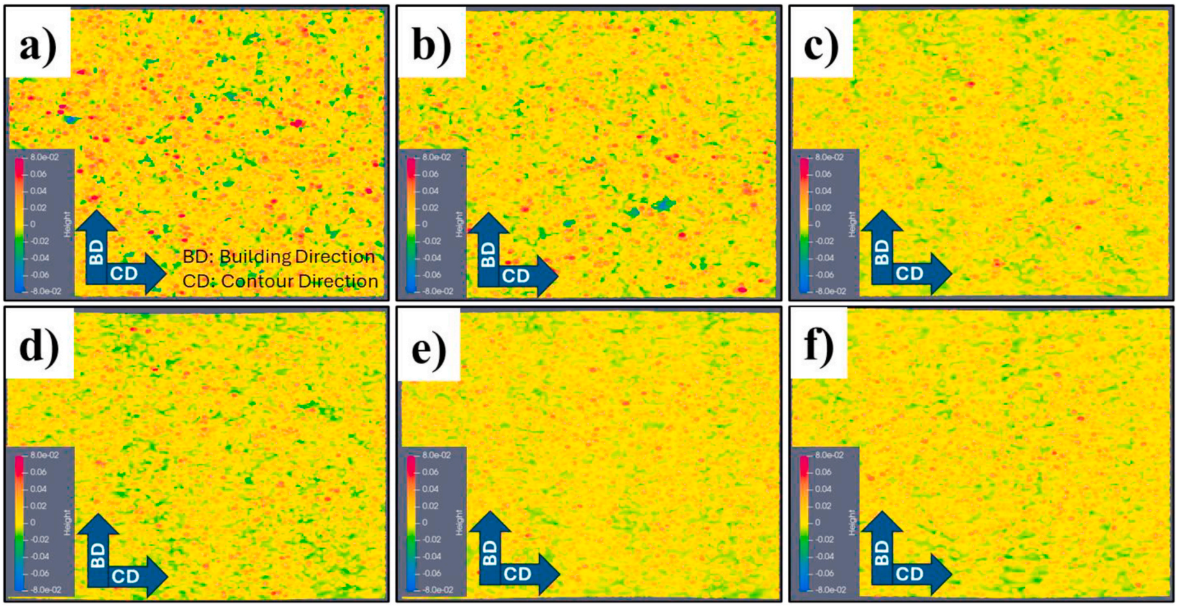

Fig. 8. Unwrapped curved surface of the samples a) P0, b) P1, c) P2, d) P3, e) P4, and f) P5.

reduced by approximately 57 % from sample P0 to P4 (Fig. 3 (a)), whereas the channel diameter for P0 and P4 samples were reduced by approximately 10 % (1077 μm–977 μm for location 1 and 1067 μm–963 μm for location 2) (Fig. 7). The channel diameter for the samples P0 to P5 is given in Figs. 5 and 6 to reveal the oversized and undersized dimensions with respect to the intended CAD design. Lee et al. has attributed the variation in dimensional accuracy of fine channels printed with high laser energy density contouring to heat accumulation and formation of wavy bulges [46]. The main reason for the reduction in diameter at higher LED contour is the wider melted region which entrains the surrounding partially melted powder particles. It can be concluded that synchronizing the designed dimensions, contour offset and contour LED is essential to simultaneously achieve a high surface quality and dimensional accuracy, as there is a trade-off among these parameters [47]. Note that the secondary process effective in achieving smoother surfaces often introduces significant dimensional change and rounding of the sharp edges of fine channels [48,49]. Therefore, it is important to account in advance for the dimensional change introduced during post-processing, in addition to those caused by due to contouring. This aspect will be addressed in future studies.

3.3. *Surface roughness measurements using XCT*

Surface profilometry and optical microscopy provide localized roughness measurements at location 1 and location 2, whereas the roughness of the entire internal curved surface can be evaluated using XCT data. As shown in the form of unwrapped internal surface in Fig. 8, the average surface roughness R_a progressively decreases from P0 to P4 (population of raddish spots), indicating that an optimal increase in laser energy density enhances the smoothness of the printed surfaces. Beyond P4, a further increase in energy density results in slightly increased roughness, likely due to dross formation, as also observed by profilometry in Fig. 4. The quantitative values of surface roughness were determined as described in the “Experimental procedure” section. The extracted point clouds representing the inner surface of the channel from XCT data is plotted along the length (building direction), as shown in Fig. 9 (a) and 9 (b) in the form of line profile for sample P0 and P5. The R_a values of each line profile were then plotted against the angle θ (0°–180°) for sample P0 to P5, as shown in Fig. 9 (c). It was observed that sample P4 exhibited the lowest R_a values (8–9 μm) among all samples, consistent with the results obtained from surface profilometry and optical microscopy. These findings indicate that XCT can be adopted as an effective technique to measure the surface roughness of curved profiles for internal channels.

3.4. *Quantitative correlation of mean surface roughness (S_a), channel diameter (CD) and LED*

Based on the above results, it was observed that surface roughness and channel diameter are significantly influenced by the LED. The surface roughness initially reduced with LED and obtained a threshold value for minimum surface roughness whereas the channel diameter progressively reduces with LED due to broadening of the melt pool. The quantitative correlation between these parameters allows to identify the optimum value of LED to achieve smoother surface with highest dimensional accuracy. The S_a vs LED relationship was obtained as follows:

$$S_a = a(\mathrm{LED})^2 + b(\mathrm{LED}) + c \tag{6}$$

S_a = Mean surface roughness, a, b, c are constants and LED = Linear energy density.

Through regression-based curve fitting of the experimental data obtained within the investigated LED range, the constants were determined as a = 481 ± 4, b = −153 ± 3 *and c* = 20. This empirical relation (Fig. 10a) can assist in the selection of LEDs for the minimisation of surface roughness. Furthermore, the relationship between channel diameter and LED follows power law as channel diameter (CD) progressively decreases with increasing LED. The empirical relationship between CD vs LED is established as follows:

$$\mathrm{CD} = p(\mathrm{LED})^n \tag{7}$$

Where p and n are constants. Regression-based curve fitting of the experimental data obtained gave $p = 911 \pm 7$ and $n = -0.035$ (Fig. 10b).

To further quantify the trade-off between surface quality improvement and dimensional reduction, the change rate of mean surface roughness (S_a) and channel diameter (CD) with respect to LED was calculated using finite differences, as exhibited in Table 3. A quantitative ratio R, as defined in eq. (8), represented the surface roughness improvement obtained per unit channel diameter reduction for a unit LED increment. A high value of R suggests the smoothening of the surface while maintaining the dimensional accuracy.

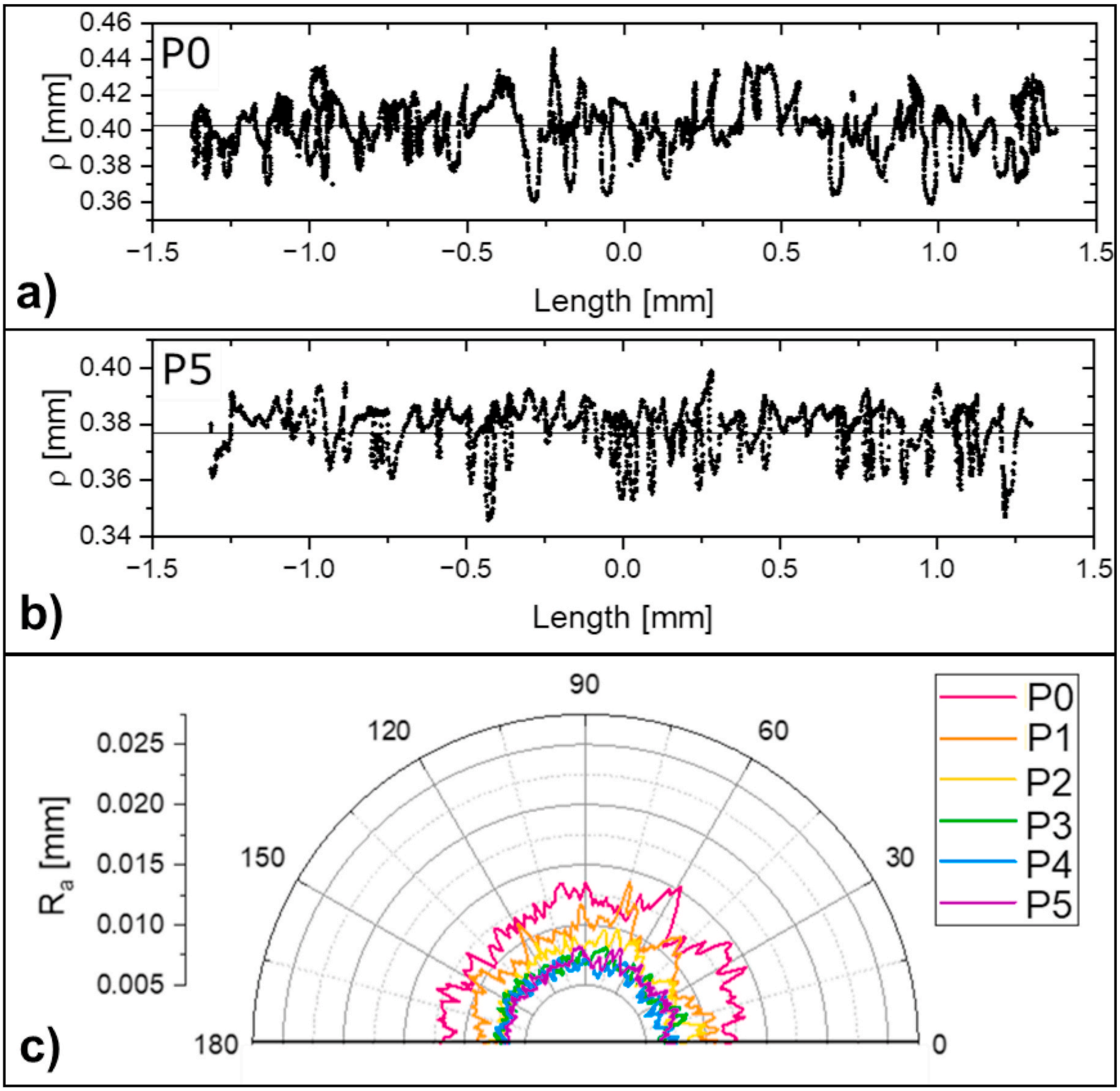

Fig. 9. Extracted cloud points of internal surface of the channel in the form of line profile along the length for sample a) P0 and b) P5. c) R_a values of the samples P0 to P5 plotted against the angle θ (0°–180°).

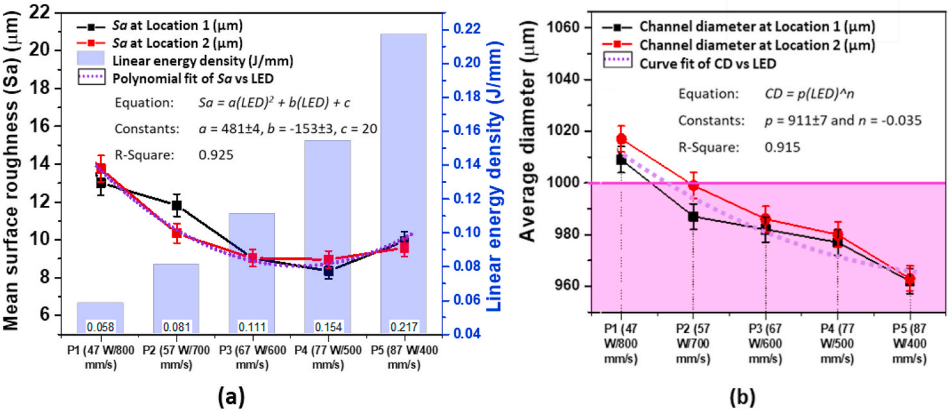

Fig. 10. Regression-based curve fitting a) Surface roughness (S_a) vs LED and b) Channel diameter (CD) vs LED.

Table 3
Quantitative trade-off analysis between surface roughness reduction and channel diameter reduction with increasing linear energy density (LED).

LED interval	ΔLED (J/mm)	ΔS_a (μm)	ΔS_a/ΔLED (μm·mm/J)	ΔCD (μm)	ΔCD/ΔLED (μm·mm/J)	R (ΔS_a/ΔCD)
0.058 → 0.081	0.023	−2.30	−100.0	−20	−869.6	0.115
0.081 → 0.111	0.030	−2.06	−68.7	−9	−300.0	0.229
0.111 → 0.154	0.043	−0.37	−8.6	−5	−116.3	0.074
0.154 → 0.217	0.063	+1.10	+17.5	−16	−254.0	0.069

$$\mathrm{R} = \left| \frac{\frac{\Delta S_a}{\Delta LED}}{\frac{\Delta CD}{\Delta LED}} \right| = \left| \frac{\Delta S_a}{\Delta CD} \right| \tag{8}$$

The analysis indicates that the LED range of 0.081–0.111 J/mm yields the maximum ratio ($R \approx 0.23$) (Table 3), suggesting that significant surface smoothening can be achieved with relatively minor dimensional loss. Beyond this range, further increases in LED result in diminishing improvement in surface roughness improvement, while channel diameter continues to decrease due to melt pool broadening. At the highest LED investigated, surface roughness begins to increase, making further LED increase unfavourable. This quantitative relationship provides a practical guideline for selecting LED values that balance surface quality enhancement with dimensional accuracy in manufacturing applications.

4. Conclusions

This study presents a systematic investigation of the influence of contour linear energy density (LED) on the internal surface quality of fine channels produced by PBF-LB. By combining surface profilometry, X-ray computed tomography (XCT), and optical microscopy (OM), a comprehensive assessment of roughness evolution was achieved. The results consistently show that increasing LED initially enhances surface finish by reducing partially fused particles and stabilizing melt-track morphology, with the lowest roughness obtained at an intermediate LED (∼0.154 J/mm). Beyond this optimal value, surface roughness increases again due to intensified balling and localized dross formation. The OM-based diameter measurements revealed that higher LED values significantly reduce channel diameter (∼1077 μm–∼962 μm) due to excessive melt-pool widening. This demonstrates a clear trade-off between surface smoothness and geometrical accuracy. A preliminary quantitative relationship between S_a reduction and diameter shrinkage was established, providing a practical guideline for contour-parameter selection. XCT enabled full-surface roughness mapping along the entire channel length, validating the trends observed by profilometry and revealing the spatial uniformity of roughness. Overall, the findings highlight that contour LED must be carefully optimized, as both insufficient and excessive energy input lead to distinct surface defects. The study demonstrates that although the minimum surface roughness was obtained at 0.154 J/mm LED value, an intermediate LED range (0.081–0.111 J/mm) provides the best balance between smooth surfaces and acceptable dimensional accuracy. These insights are directly applicable to the design of precision functional channels in aerospace, energy, and medical components.

CRediT authorship contribution statement

Jitendar Kumar Tiwari: Writing – review & editing, Writing – original draft, Software, Methodology, Data curation, Conceptualization. **Bala Malladi:** Writing – review & editing, Methodology, Investigation, Formal analysis. **Tatiana Mishurova:** Writing – review & editing, Validation, Software, Investigation. **Tobias Fritsch:** Writing – review & editing, Validation, Software, Investigation. **Lars Nyborg:** Writing – review & editing, Supervision, Project administration, Funding acquisition. **Yu Cao:** Writing – review & editing, Supervision, Project administration, Funding acquisition.

Declaration of competing interest

The authors declare that they have no known competing financial interests or personal relationships that could have appeared to influence the work reported in this paper.

Acknowledgements

The authors acknowledge competence centre TechForH2, hosted by Chalmers University of Technology Sweden, and financially supported by the Swedish Energy Agency (P2021-90268) and the member companies Volvo, Scania, Siemens Energy, GKN Aerospace, PowerCell, Oxeon, RISE, Stena Rederier AB, Johnson Matthey and Insplorion. The authors also acknowledge the funding support by Production Area of Advance, Chalmers University of Technology, Sweden, and Department of Science and Technology India under DST INSPIRE FACULTY Fellowship.

Data availability

The data that has been used is confidential.

References

[1] P. Stavropoulos, et al., Increasing the industrial uptake of additive manufacturing processes: a training framework, Advances in Industrial and Manufacturing Engineering 6 (2023) 100110.
[2] L.-Y. Chen, et al., Additive manufacturing of metallic lattice structures: unconstrained design, accurate fabrication, fascinated performances, and challenges, Mater. Sci. Eng. R Rep. 146 (2021) 100648.
[3] X. Wang, et al., Topological design and additive manufacturing of porous metals for bone scaffolds and orthopaedic implants: a review, Biomaterials 83 (2016) 127–141.
[4] J. Robbins, et al., An efficient and scalable approach for generating topologically optimized cellular structures for additive manufacturing, Addit. Manuf. 12 (2016) 296–304.
[5] C. Zhang, et al., Additive manufacturing of products with functional fluid channels: a review, Addit. Manuf. 36 (2020) 101490.
[6] S. Soller, et al., Development of liquid rocket engine injectors using additive manufacturing, in: 6th European Conference for Aerospace Sciences (EUCASS 2015), 2015.
[7] C.K. Stimpson, et al., Roughness effects on flow and heat transfer for additively manufactured channels, J. Turbomach. 138 (5) (2016) 051008.
[8] J.C. Snyder, et al., Build direction effects on additively manufactured channels 138 (5) (2016) 051006.
[9] X. Zhang, et al., Analyzing Heat Transfer Performance of ARCH Lattice Microchannel Heat Exchanger Fabricated Using Selective Laser Melting, vol. 260, 2025 124959.
[10] H. Fayazfar, et al., An overview of surface roughness enhancement of additively manufactured metal parts: a path towards removing the post-print bottleneck for complex geometries, Int. J. Adv. Manuf. Technol. 125 (3) (2023) 1061–1113.
[11] F. Careri, et al., Additive manufacturing of heat exchangers in aerospace applications: a review, Appl. Therm. Eng. 235 (2023) 121387.
[12] H. Rastan, et al., Heat transfer study of enhanced additively manufactured minichannel heat exchangers, Int. J. Heat Mass Tran. 161 (2020) 120271.
[13] H. An, et al., Unveiling the effects of laser scanning direction and processing parameters on heat transfer and ablation behavior of CFRP, Compos. B Eng. 298 (2025) 112407.
[14] H. An, et al., Fabrication and functional characteristics of micro/nano structures on the RB-SiC surface through nanosecond pulsed laser irradiation, Ceram. Int. 49 (22, Part B) (2023) 36276–36288.
[15] A. Townsend, et al., Surface texture metrology for metal additive manufacturing: a review, Precis. Eng. 46 (2016) 34–47.
[16] I. Nasser, O. Haidn, C. Manfletti, Numerical investigation of rocket engine cooling channel heat transfer for different LNG under trans-critical conditions, Int. J. Thermofluids 20 (2023) 100461.
[17] T. Zhang, L. Yuan, Interaction of contour and hatch parameters on vertical surface roughness in laser powder bed fusion, J. Mater. Res. Technol. 32 (2024) 3390–3401.
[18] T.D. Piette, et al., Influence of contour processing parameters on porosity, surface roughness, and fatigue life in laser powder bed Al-10Si-0.4Mg, J. Manuf. Process. 118 (2024) 419–431.

[19] W. Muhammad, et al., Experimental investigation and development of a deep learning framework to predict process-induced surface roughness in additively manufactured aluminum alloys, Weld. World 67 (4) (2023) 897–921.

[20] J. Hao, et al., Surface morphology evolution of GTD-450 stainless steel during laser powder bed fusion, Vacuum 213 (2023) 112107.

[21] S. Anand Kumar, et al., Effect of duplex post-processing treatment on the surface texture characteristics of AlSi10Mg alloy processed by laser powder bed fusion technique, J. Miner. Met. Mater. Soc.: J. Miner. Met. Mater. Soc. 75 (5) (2023) 1672–1683.

[22] J. Gu, et al., Effect of surface modification on the high temperature low cycle fatigue performance of LPBF 316L austenitic steel, Eng. Fract. Mech. 302 (2024) 110094.

[23] U. Ali, et al., Internal surface roughness enhancement of parts made by laser powder-bed fusion additive manufacturing, Vacuum 177 (2020) 109314.

[24] S. Rott, et al., Surface roughness in laser powder bed fusion – interdependency of surface orientation and laser incidence, Addit. Manuf. 36 (2020) 101437.

[25] J.C. Snyder, K.A. Thole, Understanding laser powder bed fusion surface roughness, J. Manuf. Sci. Eng. 142 (7) (2020).

[26] L. Cao, et al., Optimization of surface roughness and dimensional accuracy in LPBF additive manufacturing, Opt Laser. Technol. 142 (2021) 107246.

[27] J. Wegner, et al., Zr-based bulk metallic glasses in PBF-LB/M: near-polished surface quality in the as-built state 9 (3) (2024) 585–591.

[28] G.E. Bean, et al., Effect of laser focus shift on surface quality and density of Inconel 718 parts produced via selective laser melting, Addit. Manuf. 22 (2018) 207–215.

[29] C. Guo, et al., Effect of processing parameters on surface roughness, porosity and cracking of as-built IN738LC parts fabricated by laser powder bed fusion, J. Mater. Process. Technol. 285 (2020) 116788.

[30] N. Emminghaus, et al., Residual oxygen content and powder recycling: effects on surface roughness and porosity of additively manufactured Ti-6Al-4V, Addit. Manuf. 46 (2021) 102093.

[31] P. Fischmann, F. Schrauth, F. Zanger, Influence of particle size distribution on surface roughness in powder bed fusion - a contribution to increase resource efficiency, CIRP Ann. (2023).

[32] S.-J. Chang, Z.-X. Wei, Influences of the scanning strategy on surface roughness in selective laser melting, Proc. IME B J. Eng. Manufact. 236 (14) (2020) 1853–1866.

[33] E. Masiagutova, et al., Side surface topography generation during laser powder bed fusion of AlSi10Mg, Addit. Manuf. 47 (2021) 102230.

[34] F. Simoni, A. Huxol, F.-J. Villmer, Improving surface quality in selective laser melting based tool making, J. Intell. Manuf. 32 (7) (2021) 1927–1938.

[35] F. Wang, et al., A surface quality optimization strategy based on a dedicated melt-pool control via the dashed-scan contouring technique in electron beam powder bed fusion, J. Mater. Process. Technol. 330 (2024) 118445.

[36] N. Valiyakath Vadakkan Habeeb, R. Islam, K. Chou, Influence of Pre- and Post-Contouring Strategies to Downskin Sloped Surfaces in Laser Powder-Bed Fusion (L-PBF) Additive Manufacturing 17 (11) (2024).

[37] C. Pauzon, et al., Impact of contour scanning and helium-rich process gas on performances of alloy 718 lattices produced by laser powder bed fusion, Mater. Des. 215 (2022) 110501.

[38] Y. Murakami, et al., Hydrogen embrittlement mechanism in fatigue of austenitic stainless steels, Metall. Mater. Trans. 39 (6) (2008) 1327–1339.

[39] C. Pauzon, et al., Effect of argon and nitrogen atmospheres on the properties of stainless steel 316 L parts produced by laser-powder bed fusion, Mater. Des. 179 (2019) 107873.

[40] D. Nečas, P. Klapetek, Gwyddion: an open-source software for SPM data analysis, Open Phys. 10 (1) (2012) 181–188.

[41] U. Scipioni Bertoli, et al., On the limitations of Volumetric energy density as a design parameter for Selective Laser Melting, Mater. Des. 113 (2017) 331–340.

[42] T. Zhang, L. Yuan, Understanding surface roughness on vertical surfaces of 316 L stainless steel in laser powder bed fusion additive manufacturing, Powder Technol. 411 (2022) 117957.

[43] H. An, et al., Manipulating wetting State of CFRP via one-step laser micro/Nanostructuring, Small 21 (44) (2025) e06695.

[44] H. An, et al., On the surface characteristics and removability of RB-SiC composite processed by nanosecond pulsed laser, Compos. Appl. Sci. Manuf. 180 (2024) 108082.

[45] M. Jamshidinia, F. Kong, R. Kovacevic, Numerical modeling of heat distribution in the Electron beam melting® of Ti-6Al-4V, J. Manuf. Sci. Eng. 135 (6) (2013).

[46] H. Lee, et al., Influence of linear energy on side surface roughness in powder bed fusion electron beam melting process: coupled experimental and simulation study, Powder Technol. 418 (2023) 118292.

[47] C. Peng, et al., Effect of scanning tracks on the contour morphology and dimensional accuracy of the fine structure manufactured by laser powder bed fusion, Opt Laser. Technol. 179 (2024) 111270.

[48] H.M. Khan, et al., Influence of the post-processing operations on surface integrity of metal components produced by laser powder bed fusion additive manufacturing: a review, Mach. Sci. Technol. 25 (1) (2020) 118–176.

[49] E. Maleki, et al., Surface post-treatments for metal additive manufacturing: progress, challenges, and opportunities, Addit. Manuf. 37 (2021) 101619.